minerals

MDPI

Article

Limits for the Identification of Smectites Mixed with Common Minerals Based on Short-Wave Infrared Spectroscopy

Ángel Santamaría-López * and Mercedes Suárez

Departamento de Geología, Universidad de Salamanca, Plaza de la Merced s/n, 37008 Salamanca, Spain; msuarez@usal.es

* Correspondence: a.santamaria@usal.es

Abstract: The identification of minerals, particularly clay minerals, using visible, near-infrared, and short-wave infrared (VNIR-SWIR) spectroscopy has gained prominence due to its efficiency and the advancement of remote hyperspectral sensors. However, identifying minerals in polymineralic samples remains challenging due to overlapping absorption features. This study prepared systematic binary mixtures of two smectites (dioctahedral and trioctahedral) with common non-clay minerals (calcite, dolomite, gypsum, quartz, and feldspar). Spectra from these mixtures were obtained using the ASD FieldSpec 4 Hi-Res spectroradiometer and analyzed with continuum removal and second derivative preprocessing to define detection limits. These limits indicate the minimum percentage of each mineral required for clear identification in various smectite–non-clay combinations. After continuum removal, smectites are identified at ≥5%–10% in mixtures with carbonates, quartz, and feldspar, but ≥70% is needed for gypsum. Non-clay minerals have detection limits of ≥70% for calcite and 20% for gypsum in the presence of smectites, while dolomite remains undetectable. The second derivative improves these limits, enabling smectite identification at 5% in carbonate mixtures and 5%–15% in gypsum mixtures. Calcite detection limits are 65%, and dolomite can be identified at ≥65% and ≥85% with dioctahedral and trioctahedral smectites, respectively. Gypsum detection limits are reduced to 10%, while quartz and feldspar cannot be identified due to lacking absorption features.

Keywords: smectites; mineral identification; SWIR spectroscopy; detection limits; spectral analysis

check for updates

Citation: Santamaría-López, Á.; Suárez, M. Limits for the Identification of Smectites Mixed with Common Minerals Based on Short-Wave Infrared Spectroscopy. *Minerals* **2024**, *14*, 1098. https://doi.org/10.3390/min14111098

Received: 20 September 2024
Revised: 25 October 2024
Accepted: 26 October 2024
Published: 29 October 2024

Copyright: © 2024 by the authors. Licensee MDPI, Basel, Switzerland. This article is an open access article distributed under the terms and conditions of the Creative Commons Attribution (CC BY) license (https://creativecommons.org/licenses/by/4.0/).

1. Introduction

The identification of mineral content, whether in hand samples, at the outcrop level, or during the study of large areas (e.g., through remote sensing techniques), is crucial for the accurate characterization of geological materials in both fundamental research and various applied science fields, such as ore mineral exploration and geotechnical surveys [1]. Various identification techniques have been developed over the years, with spectroscopy-based methods being particularly valued for their low cost, wide range of operating conditions, and fast data acquisition [2,3]. In particular, the wavelength range between 350 nm and 2500 nm, corresponding to the visible, near infrared, and short-wave infrared (VNIR-SWIR) spectroscopy, is relevant for the characterization of carbonates, sulfates, and hydrated silicates as those from the smectites group. The absorption spectra of these minerals exhibit absorption features in this range, whose position and morphology help to distinguish each mineral phase [2–7].

However, in polymineralic samples or soils where these minerals naturally occur as mixtures, the absorption features appear together in the spectra, overlapping, distorting, and deviating from their theoretical morphology (i.e., divergence of the spectrum of each mineral separately) [8,9]. Logically, this impedes their correct allocation, hampering the adequate mineral content evaluation in different geological environments. Examples of smectites in the presence of carbonates include lacustrine environments [10,11], as the

potential role of clay minerals in carbonate nucleation seems to be demonstrated [12]; hydrothermalism [13]; soils [14]; fault rocks [15]; weathering profiles [16]; and other alteration zones. Furthermore, the study of associations between these clay minerals and carbonates is of particular interest, as they are promising targets for detecting life relics on Mars [17–19]. In this sense, it has previously been recognized that the surface of Mars should contain a high concentration of carbonates, considering paleoclimatic models that suggest the past existence of a CO_2-rich atmosphere, which would explain a warm climate phase [20]. This CO_2 likely precipitated as carbonates, which, however, are not widely distributed across the planet's surface [21,22]. A possible explanation for this apparent scarcity could be the masking of carbonates by other materials [16,20,23]. Given that the presence of clays on the planet has been confirmed [24] and that these minerals have a strong spectral signature, this group of minerals may be good candidates for obscuring the carbonates. The occurrence of smectites—sulfates assemblages is typical in evaporites [25,26], in addition to hydrothermal environments [27] and soils [28]. Associations of sulfates (gypsum, kieserite, and bassanite) with smectites have also been described on the surface of Mars [29]. On the other hand, the coexistence of smectites with quartz and/or feldspar is common, mainly in sedimentary environments, as these clay minerals are typical alteration products of tectosilicates [30].

To address the challenges associated with mineral phase identification in polymineralic samples, several preprocessing techniques have been proposed [31–35]. Some of these techniques involve the implementation of complex mathematical procedures. Hence, it is common to carry out simpler preprocessing, which allows rapid modification of the spectra to highlight the absorption features, facilitating their assignment to specific minerals. Notable among these methods are continuum removal [3,36] and the second derivative [37,38] of the original spectrum. These techniques are especially valuable when working with the large datasets of spectra generated by VNIR-SWIR spectroscopy, as its analysis equipment can be mounted on drones or transported as in situ field-acquisition instruments [39]. Both continuum removal and the second derivative are common normalization methods that simplify the comparison of different spectra by providing a shared baseline between spectra. Continuum removal is a type of background subtraction [40] that constructs a convex envelope over the original spectrum by connecting several local maxima. This process corrects differences in global reflectance between spectra while largely preserving the morphology of the original absorption features. On the other hand, plotting the second derivative of spectra has been previously used for highlighting the occurrence of sometimes partially masked features existing in the original spectra. For instance, the second derivative of the spectra tends to improve the identification of subtle shoulders that occur as peaks in the second derivative curve [37,41,42].

In this study, binary mixtures of two smectites (one dioctahedral and one trioctahedral) with various non-clay minerals were prepared to establish detection limits using VNIR-SWIR spectroscopy. The limit of detection for a component is crucial in the application of analytical techniques such as spectroscopy. The term "detection limit" generally refers in geochemistry to the lowest quantity of a substance that can be distinguished from a blank with a certain level of confidence [43]. This limit is influenced not only by the response of a component to a specific technique but also by the effects of other components on the signal. Accordingly, the "detection limit" concept has been extensively discussed in the field of spectroscopy, alongside the inherent limitations of the method [4,44]. Since the meaning of this term can vary across studies [45] and may be confused with similar concepts such as identification, determination, or blank limits [46], for this study we chose to employ "detection limit" in a qualitative sense. Specifically, we refer to the minimum percentage of a mineral in each set of prepared binary samples necessary for its identification from the spectral data. In this context, we adopt an approach similar to those used in studies involving binary mixtures and the analysis of their respective spectra [23,47,48].

The research builds on the previous work by Santamaría-López et al. [49], which focused on binary mixtures with kaolinites and established detection limits. That earlier study highlighted the surprisingly high detection limits of calcite and dolomite in the presence of

kaolinite, suggesting that carbonates might go undetected in such mineral mixtures. The spectra of the smectites are slightly more complex than that of kaolinite [5,38]. For instance, the number and position of absorption bands between 2100 nm and 2500 nm in the smectite group are directly linked to the octahedral cation composition, which justifies the use of two different smectites in this study [5,37,50]. It is anticipated that the results with smectites will differ from those with kaolinites, not only due to the variations in the number and position of spectral features but also because of differences in absorption coefficients between these groups of clay minerals. Together, both studies aim to provide a comprehensive overview of the spectroscopic behavior of the most common clay mineral groups when mixed with typical non-clay minerals.

2. Methodology

For this study, two smectites—one dioctahedral (Di-Sme) and one trioctahedral (Tri-Sme)—were mixed with five different non-clay minerals: calcite (Cal), dolomite (Dol), gypsum (Gp), quartz (Qz), and feldspar (Fsp) (non-clay minerals abbreviations according to Warr [51]). The Di-Sme sample originates from the Tamame de Sayago deposit (Zamora, Spain) (studied by García-Romero et al. [52] and Manchado et al. [53]). The Tri-Sme, referred to as ROS in García-Romero and Suárez [54], comes from the Esquivias deposit (Toledo, Spain) [55].

These minerals were gently pulverized in agate mortar to a particle size of <50 microns. While particle size influences the overall reflectance value of a spectrum, it is particularly important to note that it does not affect the relative depth of absorption features within a single spectrum [56]. In addition, since the same original samples of the pulverized minerals were used during the preparation of all the new samples, the impact of this factor is consistent among them. Each smectite was homogeneously mixed with each non-clay mineral, varying their proportions to obtain binary mixture samples, each weighing 3 g. For each combination of smectite and non-clay mineral (e.g., Di-Sme mixed with Cal; Di-Sme mixed with Dol, etc.), 19 binary samples were prepared with continuous variations in mineral proportions at 5% intervals (i.e., from 95% smectite—5% up to a sample containing 5% smectite—95% calcite). Consequently, 5 sets of binary samples were prepared with Di-Sme and the other 5 sets with Tri-Sme. Each binary sample was labeled as follows: "smectite %—non-clay mineral %", such as Di-Sme 70%—Cal 30%, for instance. In total, 190 new samples were prepared, along with 7 pure mineral samples, and all were measured using an ASD FieldSpec 4 Hi-Res to obtain their individual VNIR-SWIR spectra. The equipment operates in a wavelength range between 350 nm and 2500 nm by using three detectors (VNIR, SWIR1, and SWIR2) to cover the complete range of wavelengths, with 3 nm and 8 nm of spectral resolution in the VNIR and SWIR waveranges, respectively. Spectralon© was used as a white reference. Each sample was placed in a metallic sample holder and measured with direct contact using a contact probe, which was protected by a non-spectral glass. The final reflectance spectrum of each measured sample was the average of 25 spectra. For data visualization, Spectragryph software (version 1.2.15; Menges [57]) was used. The measurements with the equipment were conducted under normal laboratory conditions and took place over a two-day period, during which variations in relative humidity were minimal.

In addition to analyzing the raw spectra, two pre-processing methodologies were applied to the spectra: (1) the continuum removal (CR) and (2) the second derivative (SD). The continuum removal of spectra was carried out with a Python script based on the PySptools library [58]. The continuum removal of the spectra was conducted following the procedures outlined by Cardoso-Fernandes et al. [58] and Clark and Roush [3], which involve applying a hull-quotient procedure that ultimately normalizes the spectra. Initially, a convex hull is fitted by connecting points from the original spectrum that correspond to local maxima. This convex hull is subsequently removed through a hull-quotient process, where the original reflectance values are divided by the convex hull. Three delimited wavelength regions were selected for their study, and the CR applied for each separately: (1) 1255 nm–1690 nm, (2) 1800 nm–2145 nm, and (3) 2070 nm–2415 nm (Table 1). These

regions were chosen based on the occurrence of the studied minerals key absorption features [5,6,59]. Applying the CR to specific regions of each spectrum was preferable to performing it across the entire SWIR wavelength range. This approach allowed the script to achieve better normalization for each region, reaching an intensity value of 1, and enhanced the comparison between the CR spectra of binary mixture samples. Specifically, the Di-Sme includes a band at 1415 nm, whereas the Tri-Sme shows two bands lying at 1391 nm and 1413 nm. In the second wavelength region, both smectites exhibit a prominent band centered at ~1908–1910 nm, hereinafter named "~1909 nm band". In the third region, the Di-Sme shows a band at 2210 nm. Whereas in the Tri-Sme bands in this region occur at 2293 nm and 2312 nm. To compare these absorption features between the mixtures, two parameters were measured from the CR spectra: the area (S) of each absorption feature in the region and the depth (D) of their main bands. These two parameters are automatically calculated by the Python script used during continuum removal of the spectra. For Di-Sme mixtures, these depths correspond to the intensity values at ~1415 nm, ~1909 nm, and ~2210 nm; for Tri-Sme mixtures, the values are ~1391 nm, ~1909 nm, and ~2312 nm (Table 1). The area for a particular absorption feature is determined between the horizontal line at an intensity value of 1 and the curve of the CR spectrum (see Figure S1). The second derivatives of the original spectra were performed by using the ViewSpec Pro (version 6.2) software. The derived gap factor was established at 7 after conducting multiple spectral viewing tests and reviewing the study by Rinnan et al. [60] on pre-processing techniques for near-infrared spectra. These tests revealed that lower values of this parameter led to an increased noise ratio, while higher values resulted in excessive smoothing of the signal. In both instances, this hindered the accurate identification of bands. In the selected regions, the heights (D_2) of the most relevant peaks were measured from a base line at y = 0 by using the Spectragryph software. X-ray diffraction (XRD) analyses were performed with a Bruker diffractometer, D8 Advance ECO, with a LYNXEYE SSD160 high-resolution detector and Cu Kα radiation, operating at 0.05° 2 theta/s. Diffraction patterns are included in Figure S2. Most of the mineral samples are pure or almost pure, except for the Di-Sme sample containing traces of alunite (~2%), kaolinite (~2%), and the feldspar sample, which contained traces of illite (~1%).

Table 1. Wavelength regions of spectra selected for their study by continuum removal and second derivative. For each region, the main absorption bands used for the detection of each mineral are indicated.

	Region 1255 nm–1690 nm	**Region 1800 nm–2145 nm**	**Region 2070 nm–2415 nm**
Di-Sme	1415 nm	1910 nm	2210 nm
Tri-Sme	1391 nm	1908 nm	2312 nm
Calcite		1875 nm; 1995 nm	2337 nm
Dolomite			2320 nm
Gypsum	1446 nm; 1490 nm; 1535 nm	1944 nm	2175 nm; 2217 nm; 2267 nm

3. Results and Discussion

The raw spectra of the unmixed mineral samples used in this study are those typical for each mineral (Figure S3) [2,5,61]. The description of their characteristic absorption bands has been included in the Supplementary Material document. Additionally, for reason of visual clarity, in the following figures only a selection of mixture spectra (i.e., 90%–10%, 80%–10%, up to 10%–90%) is included for each set of both smectites mixed with calcite, dolomite, and gypsum. Figures showing overlapped spectra of the complete range of mineral proportions (including mixtures with quartz and feldspar) are in Supplementary Material (Figures S4–S13 and S15–S19).

3.1. SWIR Spectra of the Binary Mixture Samples

The reflectance spectra of binary samples containing both Di-Sme and Tri-Sme mixed with calcite, dolomite, and gypsum are shown in Figure 1, Figure 2, and Figure 3, respectively. For clarity, the spectra are displayed with offsets, and the wavelength range is restricted between 850 nm and 2500 nm as the characteristic absorption features of the studied minerals fall within this range. Changes in the proportions of the minerals result in morphological differences compared to the end-member spectra (i.e., the spectra obtained from the samples of the minerals used to create the mixtures). These morphological changes primarily involve variations in the sharpness of the bands and modification in the slope of their flanks, as well as fluctuations in reflectance values—either increasing or decreasing—both within the bands and in the band-lacking sections (e.g., between 1200 nm and 1300 nm in the Di-Sme—Cal set, Figure S4a).

As the calcite content increases, the bands at 1415 nm, 2210 nm (Di-Sme), and 2312 nm (Tri-Sme), as well as the ~1909 nm bands, initially experience a slight decrease in reflectance values, followed by a continuous increase (Figure S4). A similar pattern of an initial reflectance drop followed by an increasing trend is observed in the Tri-Sme—Dol set (Figure S5b), whereas no such drop occurs in the Di-Sme—Dol set (Figure S5a). However, despite these variations, the monitored absorption features are mostly identifiable even in samples with lower clay mineral contents. But it is noticeable that the sharpness of some bands decreases if the smectite content is too low. For example, the 2293 nm band in the Tri-Sme spectrum is mostly identifiable as a shoulder if the smectite content drops (Figure 1b). These shoulders are still indicating the occurrence of Tri-Sme in the mixture, especially if they are accompanied, as is the case, by the other typical bands of the mineral.

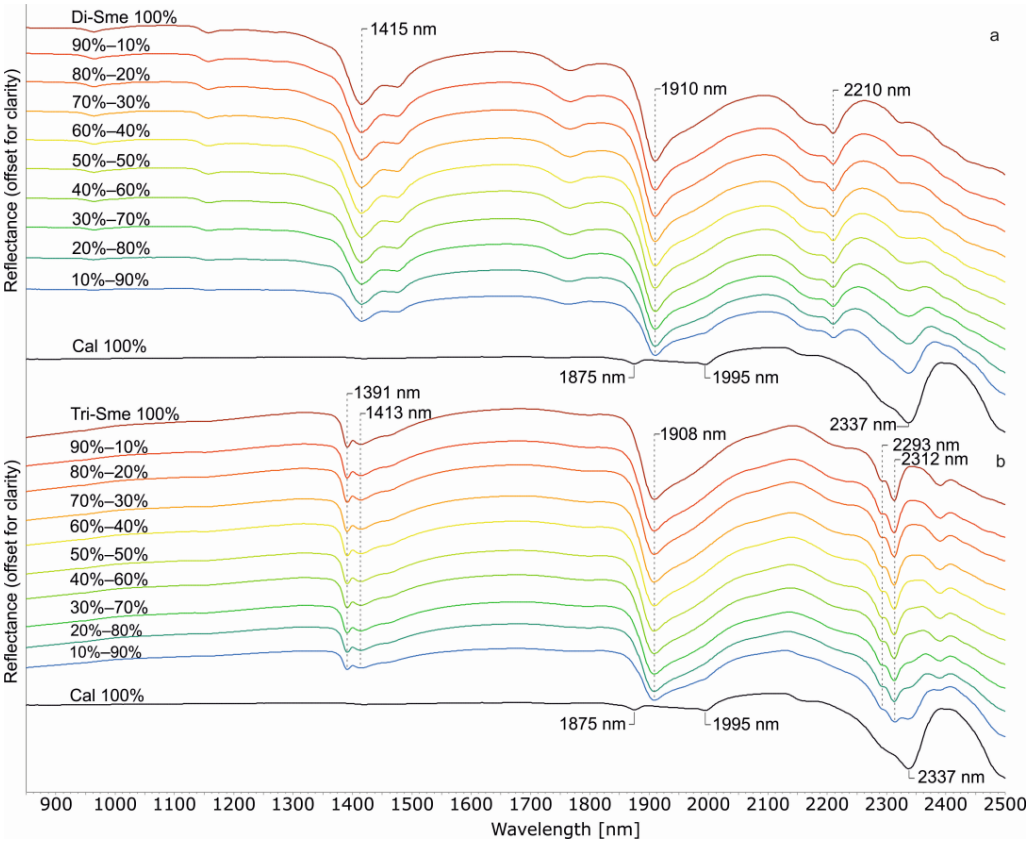


Figure 1. SWIR spectra of binary mixture samples of dioctahedral smectite with calcite (Di-Sme—Cal) (**a**), and trioctahedral smectite with calcite (Tri-Sme—Cal) (**b**). The spectra are offset for clarity.

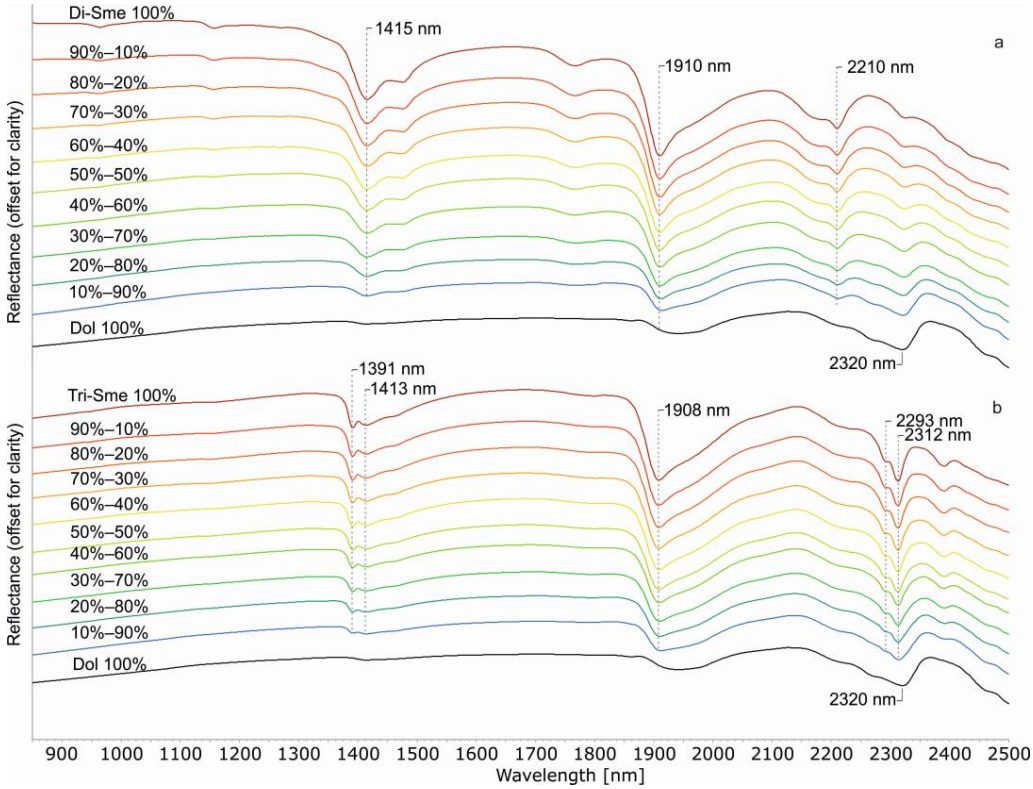


Figure 2. SWIR spectra of binary mixture samples of dioctahedral smectite with dolomite (Di-Sme—Dol) (**a**), and trioctahedral smectite with dolomite (Tri-Sme—Dol) (**b**). The spectra are offset for clarity.

The calcite bands at 1995 nm and the broad feature of the dolomite spectrum centered at 1940 nm affect the geometry of the right flank of the ~1909 nm band of both smectites by introducing a shoulder at ~2000 nm (Figure 1). However, the distinctive fingerprint of the smectites is more dominant in this region and strongly hampers the use of these bands as indicators of calcite or dolomite presence. Only in the mixtures of Di-Sme 10%—Cal 90% and Tri-Sme 10%—Cal 90% does the small shoulder at 1995 nm potentially indicate the presence of calcite (see Figure 1). The 2337 nm band of calcite significantly influences the geometry of the clay spectra at these wavelengths, as noted by Mulder et al. [62], among others. This impact increases the sharpness of the Di-Sme spectrum (e.g., observe how the right flank of the 2337 nm band progressively changes the slope of the curve around ~2355 nm; Figure 1a) and strongly alters the right flank of the 2312 nm band in the Tri-Sme spectrum. The 2320 nm feature of dolomite roughly coincides with a small band in the Di-Sme spectrum in that region (Figure 2a), and, similar to calcite, variations in the mineral proportions affect the slopes of the spectra. The Tri-Sme band at 2312 nm mostly overlaps with the 2320 nm band of dolomite (Figure 2b), hampering the identification of the carbonate. Finally, no significant drifts are observed in the position of the smectite bands in mixtures with either carbonate (Figures 1 and 2). The preservation of these positions is advantageous for smectite identification, as logical.

The interaction between the spectra of these clay minerals and gypsum (Figure 3) leads to severe morphological modifications (as illustrated by Robertson et al. [9]), more remarkable than in the case of carbonates. This is particularly evident between the smectite bands at ~1400 nm and the sulfate bands occurring at 1446 nm, 1490 nm, and 1535 nm, as the spectral fingerprint of gypsum tends to dominate the curve shapes in this region. Additionally, the gypsum band at 1944 nm obscures the ~1909 nm band of both smectites. Furthermore, a reduction in the presence of the 2293 nm and 2312 nm bands in the Tri-Sme spectrum is observed, along with an increase in its reflectance value. The partial overlap of the Di-Sme and gypsum bands around ~2200 nm, coupled with shifts in band positions

in this region, complicates the differentiation of these minerals. The Tri-Sme induces an increase in the slope of the gypsum spectrum between 900 nm and 1200 nm, progressively obscuring the two characteristic gypsum bands at 1000 nm and 1200 nm. In mixtures containing Di-Sme, variations in overall reflectance are observed in the same region, but without significant changes in slope. However, the presence of Di-Sme does alter the positions of the gypsum bands at 1000 nm and 1200 nm. The analysis of sulfate spectrum slopes in this wavelength range has previously been used to estimate the hydration state of these minerals, allowing for the differentiation between gypsum, bassanite, and anhydrite. For instance, this method has been employed to identify the composition of fractures formed by meteoritic impacts, which were subsequently filled by low-temperature aqueous fluids [63]. In this context, the presence of Tri-Sme would significantly alter the expected gypsum slope, complicating its accurate interpretation. Indeed, the positive slope induced by Tri-Sme more closely resembles the spectra of anhydrite and/or bassanite, as shown in Squyres et al. [63].

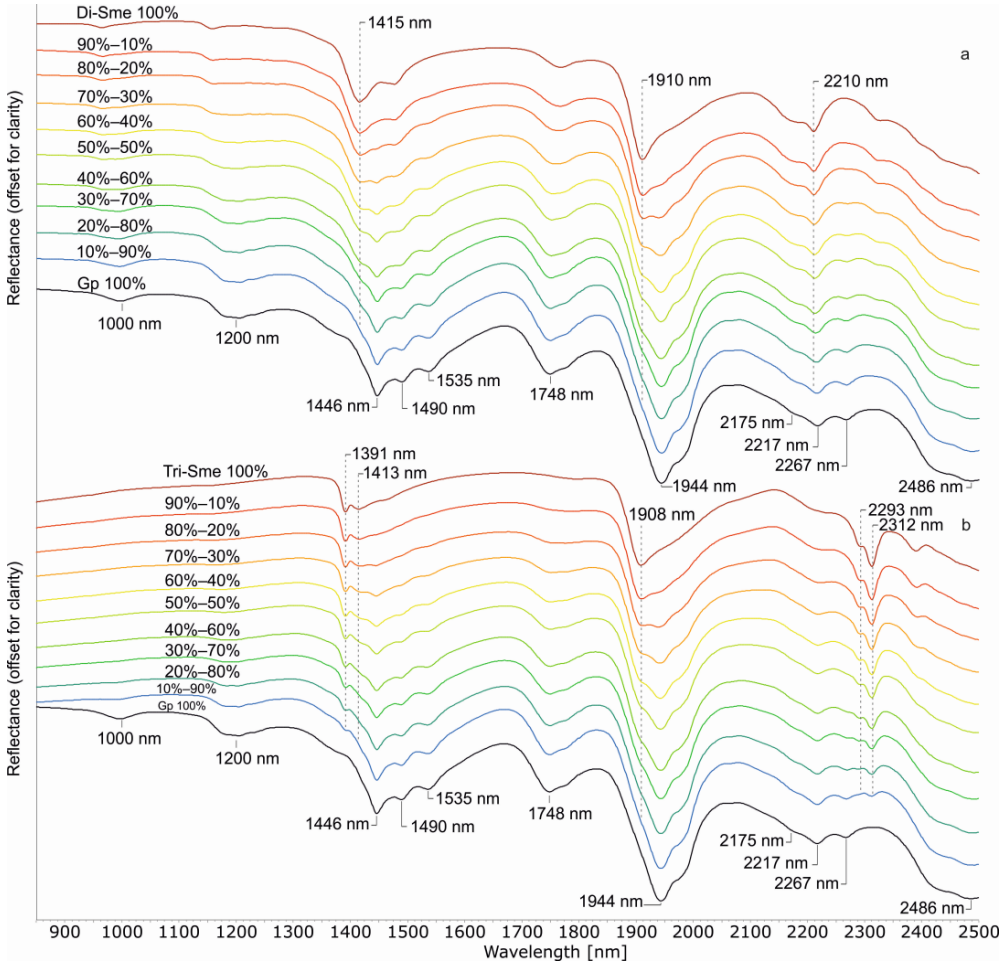


Figure 3. SWIR spectra of binary mixture samples of dioctahedral smectite with gypsum (Di-Sme—Gp) (**a**), and trioctahedral smectite with gypsum (Tri-Sme—Gp) (**b**). The spectra are offset for clarity.

The interference of quartz and feldspar spectra with both smectites is more limited compared to other mixtures discussed earlier, due to the absence of distinctive absorption features in these tectosilicate spectra. Notable changes as the content of tectosilicates increases include a decrease in the depth of smectite absorption features (e.g., the ~1909 nm band in Figures S7 and S8) and a reduction in the global reflectance value in regions lacking specific bands (e.g., between 1600 nm and 1700 nm, Figures S7 and S8).

Ultimately, an increase in gypsum content has a more pronounced effect on the original spectral geometry of the smectites than mixtures with calcite, dolomite, quartz, or feldspar. As logical, the spectra of binary samples tend to more closely resemble that of the endmember with the highest proportion of that mineral in the mixture (as reported by Zhang et al. [64], Bou-Orm et al. [65], Ducasse et al. [66], McKeown et al. [67], among others). However, certain remarkable features remain observable even in low-content mixtures. For example, smectite features in carbonate-rich mixtures are still evident, such as the ~1400 nm band and the ~1909 nm band in the Di-Sme 10%—Cal 90% sample (Figure 1a).

3.2. CR Spectra of the Binary Mixture Samples

The application of continuum removal in the analyzed regions facilitates a more accurate comparison between mixtures (see Figures 4–6 and Figures S9–S13). This approach is further supported by measurements of intensity at key wavelengths (D) and the areas of the examined features (S). Diagrams illustrating the variation of these parameters relative to the non-clay mineral content (in %) are provided in Figure S14. The trends previously discussed in Section 3.1—such as changes in band depths and the overall morphology of absorption features, which diverge from the unnormalized spectra—remain largely consistent after applying the continuum removal.

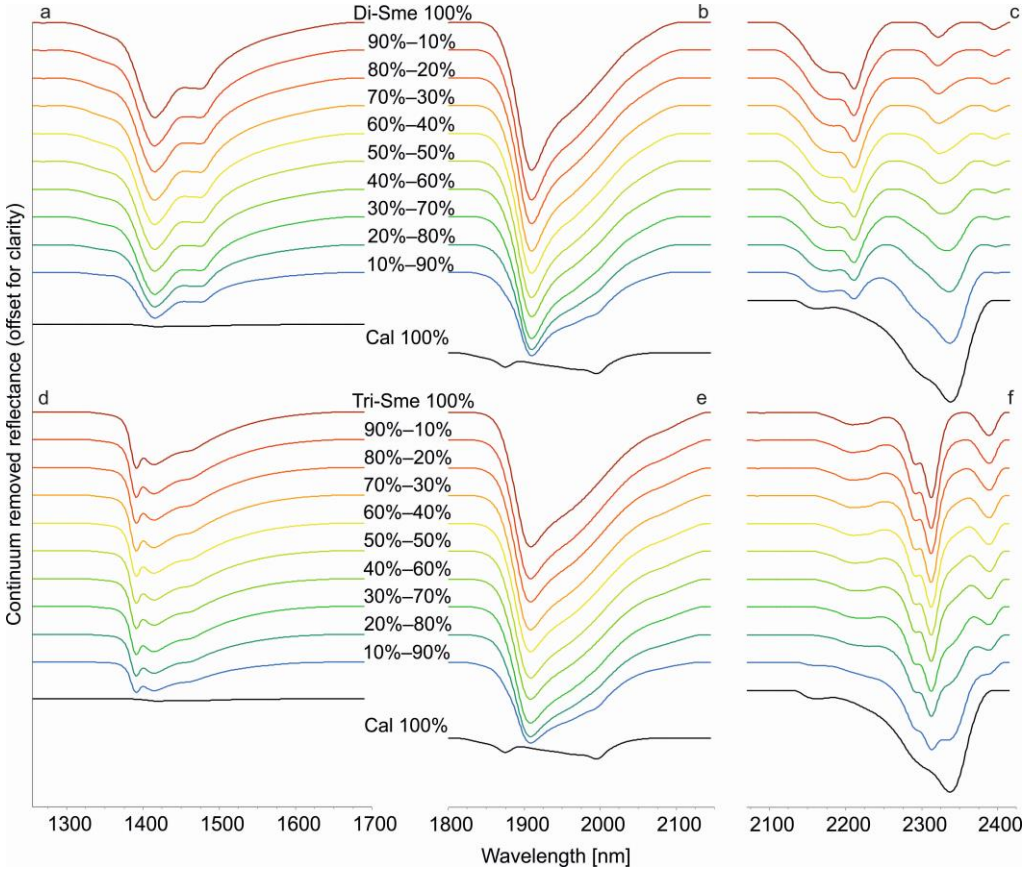


Figure 4. Continuum removed-spectra regions of binary mixture samples of dioctahedral smectite with calcite (Di-Sme—Cal) (**a**–**c**); and trioctahedral smectite with calcite (Tri-Sme—Cal) (**d**–**f**). The CR spectra are offset for clarity.

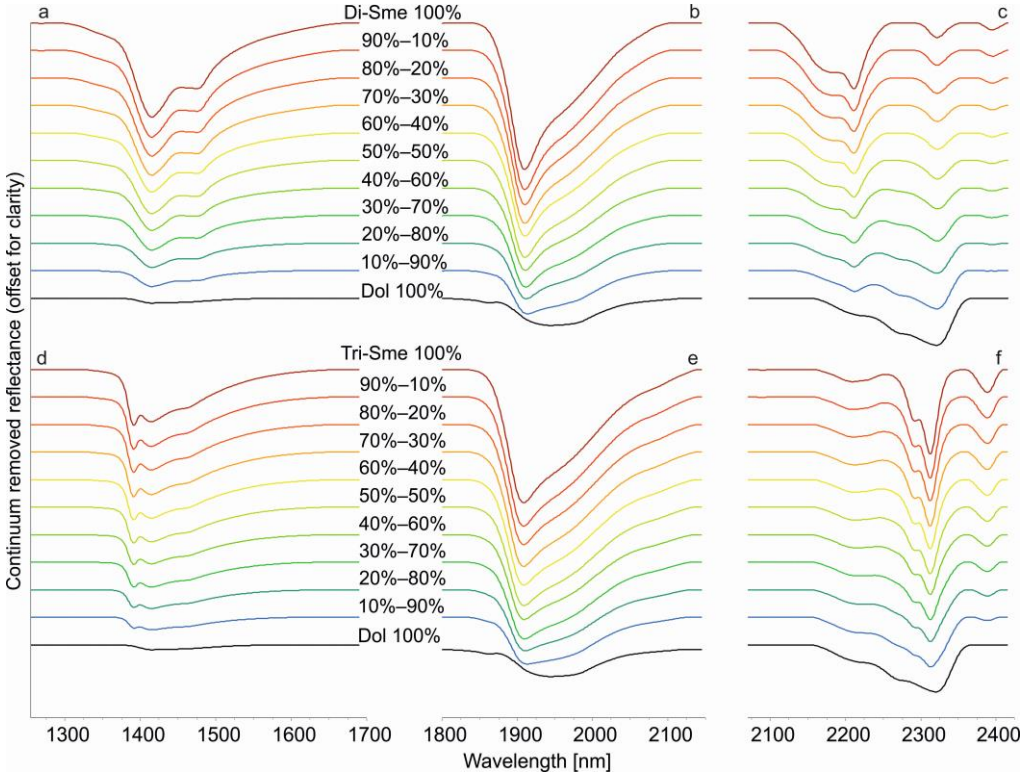


Figure 5. Continuum removed-spectra regions of binary mixture samples of dioctahedral smectite with dolomite (Di-Sme—Dol) (**a**–**c**); and trioctahedral smectite with dolomite (Tri-Sme—Dol) (**d**–**f**). The CR spectra are offset for clarity.

At a glance, calcite and dolomite cause a decrease in both D and S of the absorption features included in the 1255 nm–1690 nm and 1800 nm–2145 nm regions (see Figure 4a,b,d,e and Figure 5a,b,d,e). Comparatively, the 2210 nm and 2312 nm bands exhibit more complex morphological changes as the carbonate content increases (Figure 4c,f). Identifying Di-Sme in mixtures with calcite is straightforward since the 1415 nm, ~1909 nm, and 2210 nm bands are well preserved, even in mixtures with the highest carbonate proportions (see Figure 4a,b). Therefore, the minimum detectable content of Di-Sme is ≥5% (see Figure S9). Identifying Tri-Sme is somewhat more challenging due to the distortion of the 2312 nm band by the calcite absorption feature in this region (see Figure 4f). With ≥10% Tri-Sme, it is possible to determine the presence of this smectite. The calcite band at 1995 nm is detectable in mixtures with either smectite when the calcite content is ≥90%, while the 1875 nm band is discernible with ≥95% calcite (see Figure 4b,e and Figure S9b,e). Consequently, the identification of calcite primarily relies on the 2337 nm band. In mixtures with Di-Sme, this band shifts to lower wavenumbers by up to ~17 nm. In the Di-Sme 30%—Cal 70% mixture, the calcite band approximately retains its original position (see Figure 4c), so a ≥70% calcite content is necessary for its identification with Di-Sme. For mixtures with Tri-Sme, the curvature of the 2337 nm band changes from convex to concave as contents vary, requiring ≥70% calcite content for accurate identification.

In samples containing dolomite, both smectites can be identified with a content of ≥10%, as the position and morphology of the observed bands are well preserved (Figure 5). The use of continuum removal does not necessarily enhance the identification of dolomite in these mixtures. The overlap of the 2320 nm band feature of dolomite with bands of both smectites in this region makes it nearly impossible to definitively assign the absorption feature to the carbonate.

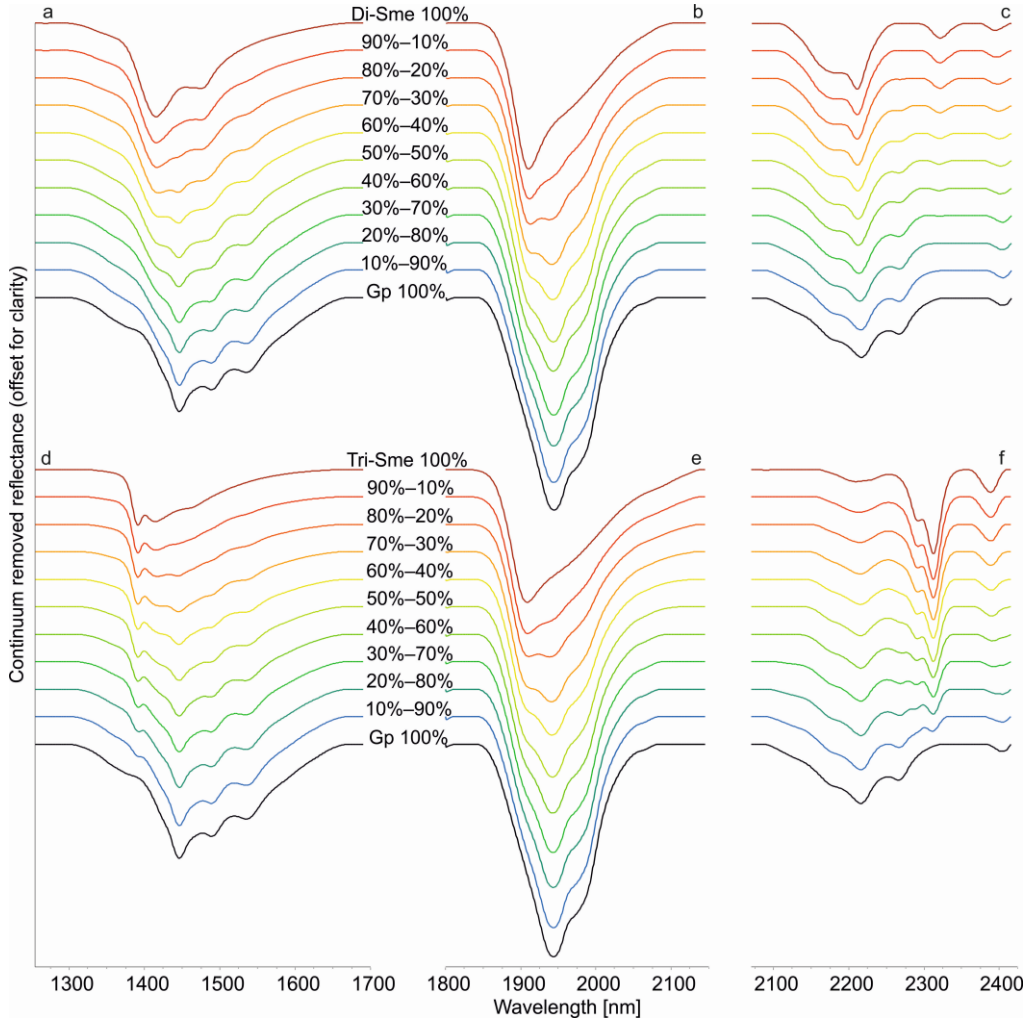


Figure 6. Continuum removed-spectra regions of binary mixture samples of dioctahedral smectite with gypsum (Di-Sme—Gp) (**a**–**c**); and trioctahedral smectite with gypsum (Tri-Sme—Gp) (**d**–**f**). The CR spectra are offset for clarity.

As discussed in Section 3.1, identifying smectites becomes significantly challenging in the presence of gypsum. Unfortunately, continuum removal does not provide a definitive method for distinguishing the absorption features of clay minerals from those of sulfates. Similar morphological modifications can be addressed for both Di-Sme and Tri-Sme sets. Thus, the bands at 1415 nm (Di-Sme, Figure 6a), 1391 nm (Tri-Sme, Figure 6d), 1413 nm (Tri-Sme, Figure 6d), and ~1909 nm (Di-Sme and Tri-Sme, Figure 6b,e) gradually evolve from sharp peaks into shoulders and finally disappear as gypsum content increases. Other bands such as 2210 nm (Di-Sme, Figure 6c) and 2293 nm (Tri-Sme, Figure 6f) exhibit a more pronounced modification, showing a lateral shift (ranging from 5 nm to 13 nm) due to progressive merging with adjacent gypsum bands. For example, the local minima at 2210 nm in the 100% Di-Sme curve (Figure S11c) migrates laterally towards higher wavelength values until the curve reproduces the gypsum band (100%). These shifts should be interpreted as apparent since the band positions of the end-members do not change. Thus, any observed displacement is solely due to the merging of nearby bands from the two minerals. On the other hand, the band at 2312 nm of Tri-Sme maintains its position (Figure 6f), resulting in a key band for the identification of the clay mineral. In summary, most of the characteristic absorption features of smectites are modified by the gypsum spectrum. Reliable identification is only feasible if the smectites contents are $\geq$70%, as most of their characteristic bands can be accurately assigned, even though they appear as

shoulders on the flanks of gypsum bands. Given the gypsum's spectral fingerprint is more dominant, its identification is possible if its proportion is ≥20%. Finally, the increase in quartz and feldspar content progressively blurs the characteristic absorption features of smectites; however, these features remain distinguishable even in samples with as little as 5% clay minerals in the CR spectra (Figures S12 and S13).

3.3. Second Derivative of Binary Mixture Samples Spectra

The second derivatives of the mixture sets are shown in Figures 7–9 and S15–S19. Calculating the second derivative of the original spectra enhances the comparison between mixtures, already described in studies such as Bishop et al. [37], Madejová et al. [38], Santamaría-López et al. [49], among others. This is because several bands and shoulders in the unmodified spectra are highlighted as second derivative peaks and tend to appear individualized from other adjacent peaks. Additionally, these second derivative peaks remain identifiable even when the proportions of minerals in the mixture change. For instance, while the Tri-Sme band at 2293 nm becomes blurred with increasing calcite content in the non-normalized spectrum (Figure 1b), a distinct second derivative peak appears at 2289 nm (Figure 7f), even in the sample containing only 10% smectite. Furthermore, within the same set, the positions of most significant peaks generally remain consistent, which aids in comparing spectra of different mixtures and accurately identifying the peaks. Despite these general improvements, the identification of mixed minerals after the second derivative is not free of difficulties in some of the sets studied. The most notable change in the smectite peaks with increasing proportions of non-clay minerals is a decrease in peak height (D_2 value) (Figure S20). By monitoring the variations in D_2 for each set of mixtures, we can infer differences in the ability of the non-clay minerals to attenuate the second derivative peaks of the smectites. Thus, the decrease in D_2 follows either exponential or linear trends (particularly in mixtures with dolomite, gypsum, quartz, and feldspar) and is comparatively more asymptotic in mixtures with calcite (though not exclusively, as seen in the Tri-Sme + Fsp curve in Figure S20f). Asymptotic curves suggest that these non-clay minerals have a lower "opacification capacity", meaning that a greater proportion of the non-clay mineral is required in the mixture for its effect on D_2 to be significant.

Despite the decrease in D_2, the identification, from their respective peaks, of Di-Sme and Tri-Sme in the mixtures with calcite and dolomite is possible with a smectite content ≥5% (Figures S15 and S16), improving or matching the identification limits obtained from CR spectra. The identification capacity of calcite is slightly improved with respect to the spectra treated with continuum removal, as the necessary calcite content is ≥65%. This improvement is attributed to better-defined peaks at 1874 nm and 1995 nm, which are now distinct from the peak at ~1909 nm of the smectites after applying the second derivative (Figure 7b,e), and the peak at 2343 nm (Figure 7c,f). Dolomite identification is also facilitated by the second derivative, with a necessary content of ≥65% in mixtures with Di-Sme and ≥85% in mixtures with Tri-Sme. In both cases, identification lies on monitoring peaks at 2266 nm or 2327 nm (Figure 8c,f and Figure S16c,f).

The identification of smectites in the presence of gypsum is significantly improved compared to CR spectra, with the minimum necessary content for Di-Sme reduced to ≥15% and for Tri-Sme to ≥5%. Several key peaks contribute to this enhancement: 1412 nm, 1905 nm, 2210 nm, and 2319 nm for the Di-Sme; and 1390 nm, 1410 nm, 1902 nm, 2289 nm, and 2312 nm for the Tri-Sme (Figure 9). An improvement in gypsum identification is also observed, with a detection limit of ≥10%. In the presence of quartz or feldspar, the detection limit for both smectites remains consistently achievable (≥5%).

Finally, the observed improvements provided by the second derivative, by enhancing the detection of the key absorption bands, are in line with the results of Mathian et al. [68] in their study of prepared binary mixtures of phyllosilicates (kaolinite, smectite, muscovite, Fe-Mg chlorite, clinochlore, and talc) for simulating lateritic saprolites.

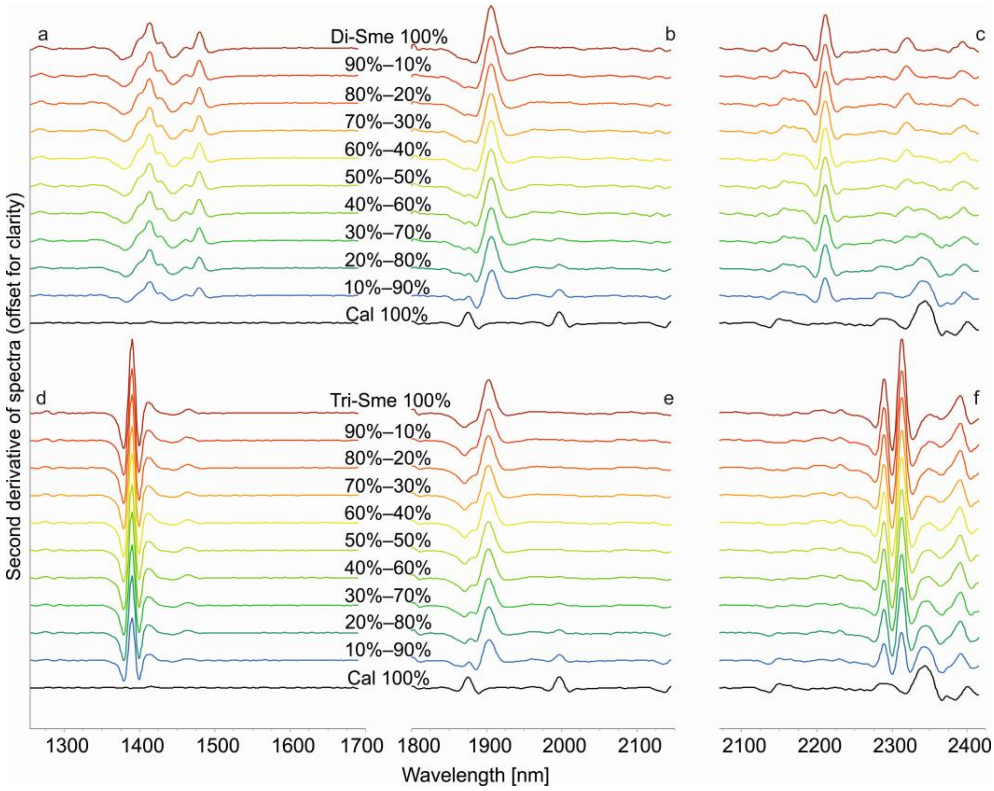


Figure 7. Second derivative of spectra regions of binary mixture samples of dioctahedral smectite with calcite (Di-Sme—Cal) (**a**–**c**); and trioctahedral smectite with calcite (Tri-Sme—Cal) (**d**–**f**). The second derivatives are offset for clarity.

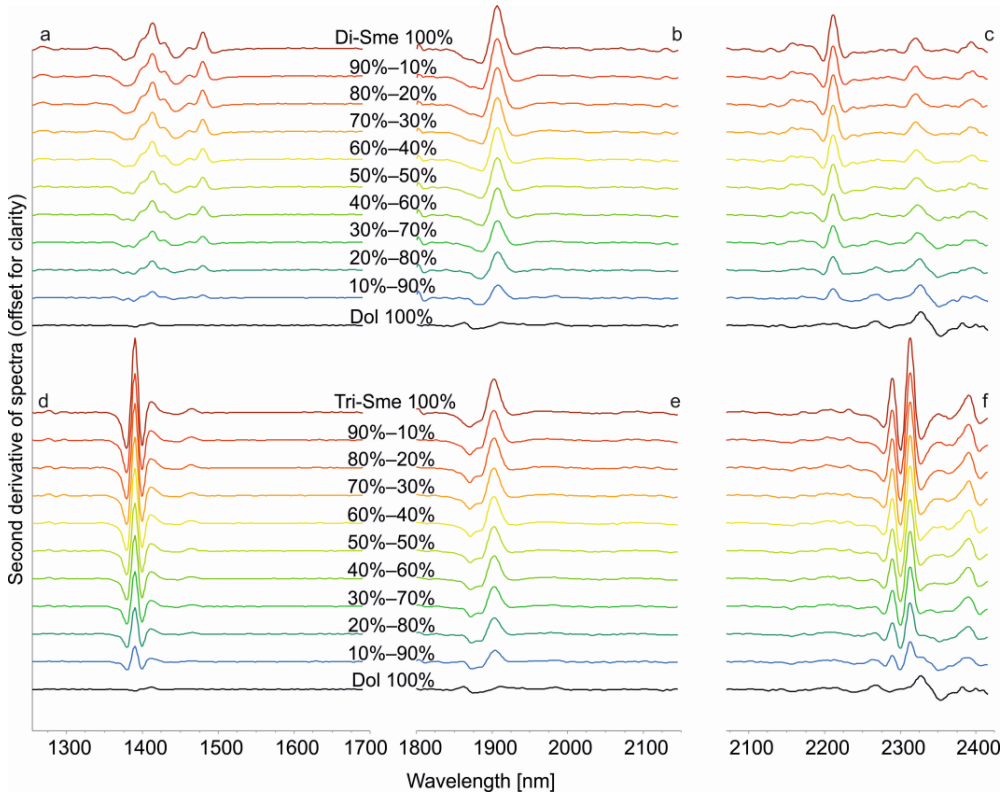


Figure 8. Second derivative of spectra regions of binary mixture samples of dioctahedral smectite with dolomite (Di-Sme—Dol) (**a**–**c**); and trioctahedral smectite with dolomite (Tri-Sme—Dol) (**d**–**f**). The second derivatives are offset for clarity.

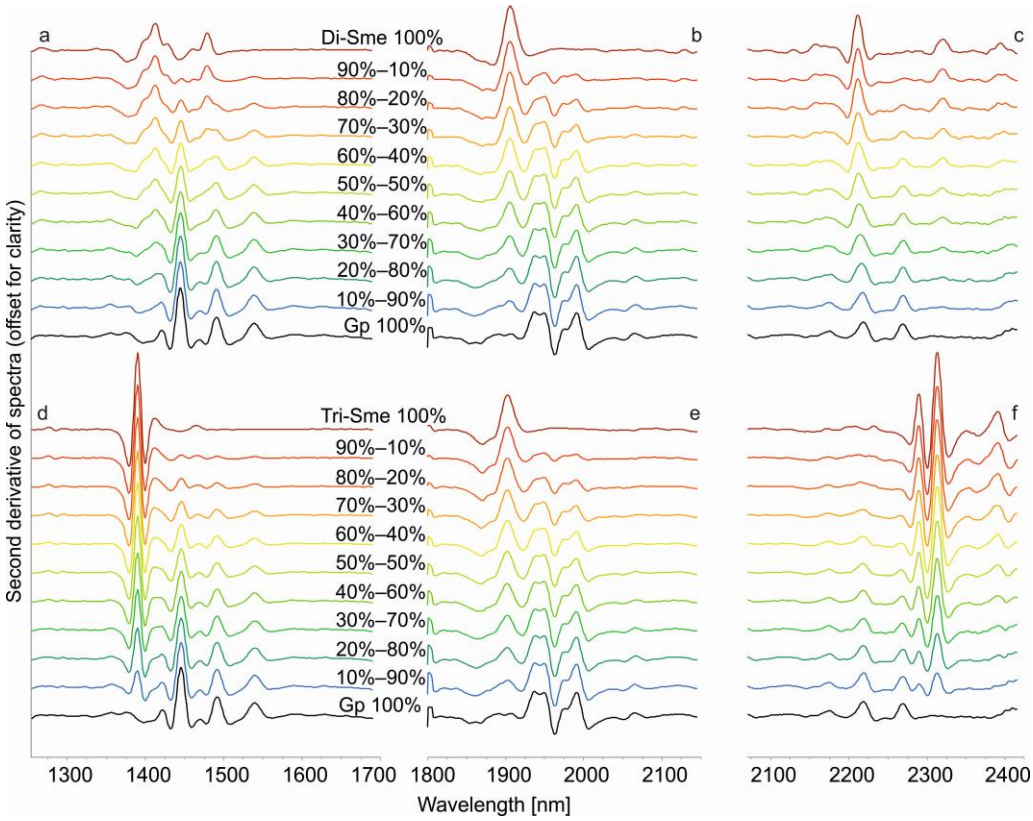


Figure 9. Second derivative of spectra regions of binary mixture samples of dioctahedral smectite with gypsum (Di-Sme—Gp) (**a**–**c**); and trioctahedral smectite with gypsum (Tri-Sme—Gp) (**d**–**f**). The second derivatives are offset for clarity.

3.4. Mineral Identification Limits

Table 2 summarizes the detection limits for minerals, showing the minimum amount (expressed as a percentage) required for accurate identification. For example, the minimum content for identifying the studied Tri-Sme in mixtures with calcite after the continuum removal preprocessing is 10% (Table 2). It is important to note that these values are constrained by the mixtures, which were prepared with continuous variations in mineral proportions at 5% intervals. Consequently, in real-world scenarios (i.e., under natural conditions), these limits may differ, as the proposed thresholds are experimentally constrained. In real-world cases, various factors can significantly affect the detection limits, including not only the number of constituents in the sample but also factors such as sample humidity (which can notably affect the intensity of the ~1909 nm band; see Robertson et al. [9]), the crystallinity of the mineral constituents, and others.

The results indicate that carbonates are notably difficult to identify, while they do not significantly impede the identification of smectites. The most challenging case is dolomite, whose identification is not feasible either in raw spectra or after continuum removal. Identification of dolomite is only possible after applying second derivative normalization and only if the carbonate content exceeds 65% and 85% for Di-Sme and Tri-Sme mixtures, respectively (see Table 2). In this regard, Ducasse et al. [66] reported that the absorption features of montmorillonite (Di-Sme) start to vanish when the calcite content ranges between 80% and 100% in binary mixtures including both minerals. Conversely, Hubbard et al. [69] estimated the content in mixtures of calcite, dolomite, and montmorillonite (25%, 25%, and 50%, respectively), and calcite and montmorillonite (80% and 20%), based on characterization algorithms applied to normalized spectra with continuum removal. The overlap of features in key areas for the identification of carbonates (1875 nm and 1995 nm; and between 2320 nm and 2340 nm) is detrimental, particularly when their spectral signature is much weaker compared to that of smectites. The high detection limits of carbonates presented

may explain the challenges in identifying these materials during remote sensing studies on Mars by using the SWIR region [16,20]. According to these results, even if carbonates were predominant in a region, a surface layer of fine materials rich in smectite—such as those resulting from the alteration of extrusive igneous rocks in surrounding areas—could effectively conceal the presence of these carbonates. For reliable detection of carbonates in the presence of smectites, it is advisable to focus on higher wavelength regions. For instance, one should monitor for the occurrence of absorption features in the range of 3400 nm to 3800 nm, which are characteristic of carbonates [16].

Table 2. Dioctahedral smectite (Di-Sme), trioctahedral smectite (Tri-Sme) and non-clay minerals (calcite, Cal; dolomite, Dol; gypsum, Gp; quartz, Qz; feldspar, Fsp) detection limits in the binary mixtures sets. Each value corresponds to the minimum content (%) of each mineral necessary for allowing its identification from the spectra sets after continuum removal and second derivative. "NI" means it is not possible to identify the mineral in the mixtures.

			Continuum Removal	Second Derivative
Mixture sets	Di-Sme—Cal	Di-Sme Cal	5 70	5 65
	Tri-Sme—Cal	Tri-Sme Cal	10 70	5 65
	Di-Sme—Dol	Di-Sme Dol	10 NI	5 65
	Tri-Sme—Dol	Tri-Sme Dol	10 NI	5 85
	Di-Sme—Gp	Di-Sme Gp	70 20	15 10
	Tri-Sme—Gp	Tri-Sme Gp	70 20	5 10
	Di-Sme—Qz	Di-Sme Qz	5 NI	5 NI
	Tri-Sme—Qz	Tri-Sme Qz	5 NI	5 NI
	Di-Sme—Fsp	Di-Sme Fsp	5 NI	5 NI
	Tri-Sme—Fsp	Tri-Sme Fsp	5 NI	5 NI

Moreover, it is concluded that, regardless of the mixture set, the second derivative is consistently more advantageous for mineral identification than continuum removal. Although the improvement in some sample sets may be minor (e.g., the identification limit of calcite in the Di-Sme-Cal set varies by only 5% between the two techniques), this advantage is particularly evident in mixtures containing dolomite, as mentioned earlier.

The smectite samples were selected to investigate possible differences in detection limits between dioctahedral and trioctahedral types, as both exhibit significant spectral variability in the 2200 nm to 2500 nm region. This variability has been reported as a challenge for predicting their presence in mixtures [62]. However, the results indicate that both types of smectites have similar identification limits. The only differences between the Di-Sme and Tri-Sme limits range from 5% (in calcite mixtures after continuum removal) to 10% (in gypsum mixtures after second derivative normalization) (Table 2). In summary, smectites can be identified in our study even when they are minor components in the samples, except in mixtures with gypsum, where a proportion of more than 70% of these clay minerals is required for accurate detection.

In Santamaría-López et al. [49], detection limits were determined in mixtures of kaolinite with the same non-clay minerals. As in the case of smectites, kaolinites showed low detection limits in the presence of carbonates (5% regardless of the preprocessing technique). The study also identified notably high detection limits for carbonates (75%

for calcite and 60% for dolomite) based on CR spectra; however, unlike the present study, these limits increased when applying the second derivative (up to 90% for both carbonates). Kaolinite in mixtures with gypsum was detectable at 15% content using CR spectra, which is lower than the 70% required for smectites (see Table 2). This difference arises because kaolinites, unlike smectites, lack an absorption feature at ~1909 nm (critical for identifying smectites), which is obscured by the sulfate fingerprint. Both clay mineral groups show improved identification in gypsum mixtures after applying the second derivative. The detection limits for gypsum remain consistent across studies.

As demonstrated in this study, various geometric parameters vary according to the proportions of minerals in prepared mixtures. Thus, we have been able to construct the curves presented in Figures S14 and S20. This offers a tempting foundation for a mineral quantification technique. For example, by correlating the variation in D_2 with smectite content, and based on the curves from Figures S14 and S20, one might estimate the smectite proportion in natural samples containing calcite. However, as established by Santamaría et al. [49], significant challenges soon arise. Due to the high compositional variability among smectites, primarily driven by the octahedral cation composition, spectra of smectites—even those with similar compositions—can differ significantly between them. Another example is the humidity of the sample, which can influence the D at ~1909 nm [9] across different samples containing smectite. For that, these curves should not be used as potential calibration graphs for predicting the concentrations of mineral constituents in other geological contexts. However, they are useful in providing insight into how interference occurs between the absorption features of significant minerals, as referred to in Section 3.3 regarding "opacification capacity". To the best of our knowledge and based on a methodology reliant on preparing sample sets, it is nearly impossible to develop general quantification models that can be consistently applied to different case studies. The methodology employed in this study serves only for qualitative purposes, specifically to establish the detectability limits of some mineral components and not for their quantification.

4. Conclusions

Detection limits have been determined from mixtures of smectites with various non-clay minerals. The most relevant results are as follows:

After applying continuum removal to the spectra, the detection limits for smectites in the presence of carbonates range between 5% and 10%. However, identifying smectites in mixtures with gypsum is considerably more challenging, with detection limits of 70%.

Calcite is difficult to identify in spectra after continuum removal, requiring a minimum content of $\geq$70%. Dolomite cannot be identified with confidence under these conditions.

Generally, detection limits for all studied minerals improve with the application of the second derivative to the spectra. For calcite, detection limits decrease to $\geq$65%, while dolomite can be detected with contents of $\geq$65% and $\geq$85% in mixtures with dioctahedral and trioctahedral smectites, respectively.

The difficulty in identifying carbonates in the presence of clay minerals is consistent with the findings of Santamaría-López et al. [49] for similar mixtures with kaolinites. This suggests that rocks such as marls cannot be accurately identified from hyperspectral VNIR-SWIR data and may be misinterpreted as clayey rocks. Conversely, in the presence of gypsum, clay minerals can remain unidentified even when they are the majority components, as long as the second derivative is not applied.

The identification of tectosilicates remains a significant challenge (e.g., Hubbard et al. [69]). While the occurrence of quartz and feldspar influences the definition of bands and second derivative peaks of other minerals in mixtures, their presence cannot be directly confirmed. A relevant example can be found in terrains analyzed through remote sensing, where tectosilicates coexist with smectites. In this context, a higher prevalence of smectites may indicate a more evolved terrain (e.g., indicating major weathering). However, without an accurate assessment of tectosilicate presence, this assumption could be misleading.

Finally, the identification of minerals is essential for material characterization. Some alternative techniques to spectroscopy, such as XRD [70], can often yield superior results. Traditionally, the advantages argued in favor of spectroscopy as a rival to XRD include the speed of data acquisition and the non-destructive nature of sample analysis. Additionally, preprocessing techniques such as the CR and second derivative analysis further support its application. In this context, various more complex data-processing methodologies are widely employed for mineral identification and quantification from spectra. These include modified Gaussian modeling (MGM) [31,32,35], exponential Gaussian optimization (EGO) [34], and radiative transfer models (RTMs) developed by Shkuratov et al. [33] and Hapke [71]. The advantage of using techniques like CR and second derivative analysis over more complex mathematical implementations primarily lies in their speed of application. However, based on the results obtained in this study, a critical examination of the CR and second derivative is necessary. It becomes clear—particularly in the case of CR applied to smectite–dolomite mixtures—that this time efficiency is of little value if accurate identification of important constituents as carbonates cannot be achieved.

Supplementary Materials: The following supporting information can be downloaded at: https://www.mdpi.com/article/10.3390/min14111098/s1, **Figure S1.** Diagram representing the area (S) and depth (D) of the main peaks of an absorption feature after continuum removal (CR). Both parameters are obtained by the script used for the CR of the spectra (see Section 2. Methodology). Three CR spectra have been used as examples to illustrate how both S and D vary depending on the proportions of the minerals present: Di-Sme 0%—Cal 100% (i.e., pure calcite sample), Di-Sme 5%—Cal 95% and Di-Sme 100%—Cal 0% spectrum (i.e., pure dioctahedral smectite sample). **Figure S2.** X-ray diffraction diagrams of the unmixed samples of the studied minerals. **Figure S3.** Reflectance spectra (in the range of 350 to 2500 mm) of the studied minerals. **Figure S4.** Superposed SWIR spectra of binary mixture samples of dioctahedral smectite with calcite (a), and trioctahedral smectite with calcite (b). **Figure S5.** Superposed SWIR spectra of binary mixture samples of dioctahedral smectite with dolomite (a), and trioctahedral smectite with dolomite (b). **Figure S6.** Superposed SWIR spectra of binary mixture samples of dioctahedral smectite with gypsum (a), and trioctahedral smectite with gypsum (b). **Figure S7.** Superposed SWIR spectra of binary mixture samples of dioctahedral smectite with quartz (a), and trioctahedral smectite with quartz (b). **Figure S8.** Superposed SWIR spectra of binary mixture samples of dioctahedral smectite with feldspar (a), and trioctahedral smectite with feldspar (b). **Figure S9.** Superposed continuum removed-spectra regions of binary mixture samples of dioctahedral smectite with calcite (a–c); and trioctahedral smectite with calcite (d–f). **Figure S10.** Superposed continuum removed-spectra regions of binary mixture samples of dioctahedral smectite with dolomite (a, b, c); and trioctahedral smectite with dolomite (d–f). **Figure S11.** Superposed continuum removed-spectra regions of binary mixture samples of dioctahedral smectite with gypsum (a–c); and trioctahedral smectite with gypsum (d–f). **Figure S12.** Superposed continuum removed-spectra regions of binary mixture samples of dioctahedral smectite with quartz (a–c); and trioctahedral smectite with quartz (d–f). **Figure S13.** Superposed continuum removed-spectra regions of binary mixture samples of dioctahedral smectite with feldspar (a–c); and trioctahedral smectite with feldspar (d–f). **Figure S14.** Diagrams showing the variation of depth and area of characteristic dioctahedral smectite (Di-Sme) and trioctahedral smectite (Tri-Sme) bands and doublets vs. the content in non-clay minerals in the binary mixture samples. These parameters were measured in the continuum removed-spectra. Non-clay mineral abbreviations: calcite, Cal; dolomite, Dol; gypsum, Gp; quartz, Qz; and feldspar, Fsp. **Figure S15.** Second derivative of spectra regions of binary mixture samples of dioctahedral smectite with calcite (a–c); and trioctahedral smectite with calcite (d–f). **Figure S16.** Second derivative of spectra regions of binary mixture samples of dioctahedral smectite with dolomite (a–c); and trioctahedral smectite with dolomite (d–f). **Figure S17.** Second derivative of spectra regions of binary mixture samples of dioctahedral smectite with gypsum (a–c); and trioctahedral smectite with gypsum (d–f). **Figure S18.** Second derivative of spectra regions of binary mixture samples of dioctahedral smectite with quartz (a–c); and trioctahedral smectite with quartz (d–f). **Figure S19.** Second derivative of spectra regions of binary mixture samples of dioctahedral smectite with feldspar (a–c); and trioctahedral smectite with feldspar (d–f). **Figure S20.** Diagrams showing the variation of the characteristic dioctahedral smectite (Di-Sme) and trioctahedral smectite (Tri-Sme) second derivative peaks depth vs. the content

in non-clay minerals. All the diagrams include the 2nd order polynomial trendlines (dashed lines). Non-clay mineral abbreviations: calcite, Cal; dolomite, Dol; gypsum, Gp; quartz, Qz; and feldspar, Fsp.

Author Contributions: Conceptualization, M.S.; methodology, Á.S.-L. and M.S.; formal analysis, Á.S.-L.; investigation, Á.S.-L. and M.S.; data curation, Á.S.-L.; writing—original draft preparation, Á.S.-L.; writing—review and editing, M.S.; visualization, Á.S.-L.; supervision, M.S.; project administration, M.S.; funding acquisition, M.S. All authors have read and agreed to the published version of the manuscript.

Funding: This study was supported by Junta de Castilla y León, Spain, and Fondo Europeo de Desarrollo Regional (FEDER) (grant number SA0107P20).

Data Availability Statement: The data presented in this study are available on request from the corresponding author.

Acknowledgments: We appreciate the valuable comments from the three anonymous reviewers, which greatly improved the quality of the manuscript. We acknowledge the technical support provided by the "Servicio de preparación de rocas" of Universidad de Salamanca. E. Manchado is especially recognized for helping with the spectroradiometer data acquisition.

Conflicts of Interest: The authors declare no conflicts of interest.

References

1. Hauff, P. *An Overview of VIS-NIR-SWIR Field Spectroscopy as Applied to Precious Metals Exploration*; Spectral International Inc.: Arvada, CO, USA, 2008; Volume 80001, pp. 303–403.
2. Hunt, G.R. Spectral signatures of particulate minerals in the visible and near infrared. *Geophysics* **1977**, *42*, 501–513. [CrossRef]
3. Clark, R.N.; Roush, T.L. Reflectance spectroscopy: Quantitative analysis techniques for remote sensing applications. *J. Geophys. Res.* **1984**, *89*, 6329–6340. [CrossRef]
4. Clark, R.N.; King, T.V.V.; Klejwa, M.; Swayze, G.A.; Vergo, N. High spectral resolution reflectance spectroscopy of minerals. *J. Geophys. Res.* **1990**, *95*, 12653–12680. [CrossRef]
5. Bishop, J.L.; Lane, M.D.; Dyar, M.D.; Brown, A.J. Reflectance and emission spectroscopy study of four groups of phyllosilicates: Smectites, kaolinite-serpentines, chlorites and micas. *Clay Miner.* **2008**, *43*, 35–54. [CrossRef]
6. Bishop, J.L. Visible and near-infrared reflectance spectroscopy: Laboratory spectra of geologic materials. In *Remote Compositional Analysis: Techniques for Understanding Spectroscopy, Mineralogy, and Geochemistry of Planetary Surfaces*; Bishop, J., Bell III, J., Moersch, J., Eds.; Cambridge University Press: Cambridge, UK, 2019; pp. 68–101. [CrossRef]
7. Bishop, J.L.; King, S.J.; Lane, M.D.; Brown, A.J.; Lafuente, B.; Hiroi, T.; Roberts, R.; Swayze, G.A.; Lin, J.F.; Sánchez Román, M. Spectral Properties of Anhydrous Carbonates and Nitrates. *Earth Space Sci.* **2021**, *8*, e2021EA001844. [CrossRef]
8. Post, J.L.; Noble, P.N. The Near-Infrared Combination Band Frequencies of Dioctahedral Smectites, Micas, and Illites. *Clays Clay Miner.* **1993**, *41*, 639–644. [CrossRef]
9. Robertson, K.M.; Milliken, R.E.; Li, S. Estimating mineral abundances of clay and gypsum mixtures using radiative transfer models applied to visible-near infrared reflectance spectra. *Icarus* **2016**, *277*, 171–186. [CrossRef]
10. del Buey, P.; Sanz-Montero, M.E.; Sánchez-Román, M. Bioinduced precipitation of smectites and carbonates in photosynthetic diatom-rich microbial mats: Effect of culture medium. *Appl. Clay Sci.* **2023**, *238*, 106932. [CrossRef]
11. Schrank, A.B.S.; Dos Santos, T.; Altenhofen, S.D.; Freitas, W.; Cembrani, E.; Haubert, T.; Dalla Vecchia, F.; Barili, R.; Rodrigues, A.G.; Maraschin, A.; et al. Interactions between Clays and Carbonates in the Aptian Pre-Salt Reservoirs of Santos Basin, Eastern Brazilian Margin. *Minerals* **2024**, *14*, 191. [CrossRef]
12. Molnár, Z.; Pekker, P.; Dódony, I.; Pósfai, M. Clay minerals affect calcium (magnesium) carbonate precipitation and aging, Earth Planet. *Sci. Lett.* **2021**, *567*, 116971. [CrossRef]
13. Chevrier, V.F.; Morisson, M. Carbonate-phyllosilicate parageneses and environments of aqueous alteration in Nili Fossae and Mars. *J. Geophys. Res. Planets* **2021**, *126*, e2020JE006698. [CrossRef]
14. Kowalska, J.B.; Skiba, M.; Maj-Szeliga, K.; Mazurek, R.; Zaleski, T. Does calcium carbonate influence clay mineral transformation in soils developed from slope deposits in Southern Poland? *J. Soil. Sediment.* **2021**, *21*, 257–280. [CrossRef]
15. Reijonen, H.M.; Elminen, T.; Heikkilä, P.; Kuva, J.; Jolis, E.M. Enhanced Identification of Fracture Smectites and Other Alteration Minerals Via Short-Wave Infrared Reflectance at Two Finnish Crystalline Sites, Olkiluoto and Hyrkkölä. *Rock Mech. Rock Eng.* **2024**, *57*, 4299–4332. [CrossRef]
16. Bultel, B.; Viennet, J.; Poulet, F.; Carter, J.; Werner, S.C. Detection of carbonates in Martian weathering profiles. *J. Geophys. Res. Planets* **2019**, *124*, 989–1007. [CrossRef]
17. Cloutis, E.A.; Grasby, S.E.; Last, W.M.; Léveillé, R.; Osinski, G.R.; Sherriff, B.L. Spectral reflectance properties of carbonates from terrestrial analogue environments: Implications for Mars. *Planet. Space Sci.* **2010**, *58*, 522–537. [CrossRef]
18. Michalski, J.R.; Cuadros, J.; Niles, P.B.; Parnell, J.; Rogers, A.D.; Wright, S.P. Groundwater activity on Mars and implications for a deep biosphere. *Nat. Geosci.* **2013**, *6*, 133–138. [CrossRef]

19. Cuadros, J.; Diaz-Hernandez, J.L.; Sanchez-Navas, A.; Garcia-Casco, A.; Yepes, J. Chemical and textural controls on the formation of sepiolite, palygorskite and dolomite in volcanic soils. *Geoderma* **2016**, *271*, 99–114. [CrossRef]
20. Harvey, R.P. Carbonates and Martian Climate. *Science* **2010**, *329*, 400–401. [CrossRef]
21. Bandfield, J.L.; Glotch, T.D.; Christensen, P.R. Spectroscopic identification of carbonate minerals in the martian dust. *Science* **2003**, *301*, 1084. [CrossRef]
22. Blaney, D.L.; McCord, T.B. An observational search for carbonates on Mars. *J. Geophys. Res.* **1989**, *94*, 10159. [CrossRef]
23. Alemanno, G.; Carli, C.; Serventi, G.; Maturilli, A.; Helbert, J. Study of Detection Limits of Carbonate Phases in Mixtures with Basaltic-like Fine Regolith in the MIR (1–5.5 µm) Spectral Range. *Minerals* **2023**, *13*, 764. [CrossRef]
24. Poulet, F.; Bibring, J.P.; Mustard, J.F.; Gendrin, A.; Mangold, N.; Langevin, Y.; Arvidson, R.E.; Gondet, B.; Gomez, C.; Berthe, M.; et al. Phyllosilicates on Mars and implications for early martian climate. *Nature* **2005**, *438*, 623–627. [CrossRef] [PubMed]
25. Hover, V.C.; Walter, L.M.; Peacor, D.R.; Martini, A.M. Mg-Smectite Authigenesis in a Marine Evaporative Environment, Salina Ometepec, Baja California. *Clays Clay Miner.* **1999**, *47*, 252–268. [CrossRef]
26. Bishop, J.L.; Gross, C.; Danielsen, J.; Parente, M.; Murchie, S.L.; Horgan, B.; Wray, J.J.; Viviano, C.; Seelos, F.P. Multiple mineral horizons in layered outcrops at Mawrth Vallis, Mars, signify changing geochemical environments on early Mars. *Icarus* **2020**, *341*, 113634. [CrossRef] [PubMed]
27. Çelik, M.; Karakaya, N.; Temel, A. Clay Minerals in Hydrothermally Altered Volcanic Rocks, Eastern Pontides, Turkey. *Clays Clay Miner.* **1999**, *47*, 708–717. [CrossRef]
28. Naimi, S.; Ayoubi, S.; Di Raimo, L.A.D.L.; Demattе, J.A.M. Quantification of some intrinsic soil properties using proximal sensing in arid lands: Application of Vis-NIR, MIR, and pXRF spectroscopy. *Geoderma Reg.* **2022**, *28*, e00484. [CrossRef]
29. Wilson, S.A.; Bish, D.L. Formation of Gypsum and Bassanite by Cation Exchange Reactions in the Absence of Free-liquid H 2 O: Implications for Mars. *J. Geophys. Res.* **2011**, *116*, 2011JE003853. [CrossRef]
30. Cuadros, J.; Caballero, E.; Huertas, F.J.; Jiménez de Cisneros, C.; Huertas, F.; Linares, J. Experimental alteration of vol canic tuff: Smectite formation and effect on 18O isotope compo sition. *Clays Clay Miner.* **1999**, *47*, 769–776. [CrossRef]
31. Sunshine, J.M.; Pieters, C.M.; Pratt, S.F. Deconvolution of mineral absorption bands: An improved approach. *J. Geophys. Res.* **1990**, *95*, 6955–6966. [CrossRef]
32. Sunshine, J.M.; Pieters, C.M. Estimating Modal Abundances From the Spectra of Natural and Laboratory Pyroxene Mixtures Using the Modified Gaussian Model. *J. Geophys. Res.* **1993**, *98*, 9075–9087. [CrossRef]
33. Shkuratov, Y.G.; Kreslavsky, M.A.; Ovcharenko, A.A.; Stankevich, D.G.; Zubko, E.S.; Pieters, C.; Arnold, G. Opposition Effect from Clementine Data and Mechanisms of Backscatter. *Icarus* **1999**, *141*, 132–155. [CrossRef]
34. Pompilio, L.; Pedrazzi, G.; Sgavetti, M.; Cloutis, E.A.; Craig, M.A.; Roush, T.L. Exponential Gaussian approach for spectral modeling: The EGO algorithm I. *Band saturation. Icarus* **2009**, *201*, 781–794. [CrossRef]
35. Rialland, R.; Soussen, C.; Marion, R.; Carrere, V. Improved Deconvolution of Mineral Reflectance Spectra. *IEEE J. Sel. Top. Appl. Earth Obs. Remote Sens.* **2021**, *14*, 9711–9726. [CrossRef]
36. Makarewicz, H.D.; Parente, M.; Bishop, J.L. Deconvolution of VNIR spectra using modified Gaussian modeling (MGM) with automatic parameter initialization (API) applied to CRISM. In Proceedings of the WHISPERS '09–1st Workshop on Hyperspectral Image and Signal Processing: Evolution in Remote Sensing, Grenoble, France, 26–28 August 2009; pp. 1–5. [CrossRef]
37. Bishop, J.L.; Madejová, J.; Komadel, P.; Fröschl, H. The influence of structural Fe, Al and Mg on the infrared OH bands in spectra of dioctahedral smectites. *Clay Miner.* **2002**, *37*, 607–616. [CrossRef]
38. Madejová, J.; Gates, W.P.; Petit, S. IR Spectra of Clay Minerals. In *Developments in Clay Science*; Gates, W.P., Kloprogge, J.T., Madejová, J., Bergaya, F., Eds.; Elsevier: Amsterdam, The Netherlands, 2017; pp. 107–149. [CrossRef]
39. Novais, J.J.; Poppiel, R.R.; Lacerda, M.P.C.; Demattê, J.A.M. VNIR-SWIR Spectroscopy, XRD and Traditional Analyses for Pedomorphogeological Assessment in a Tropical Toposequence. *Agric. Eng.* **2023**, *5*, 1581–1598. [CrossRef]
40. Hecker, C.; van Ruitenbeek, F.J.A.; van der Werff, H.M.A.; Bakker, W.H.; Hewson, R.D.; van der Meer, F.D. Spectral Absorption Feature Analysis for Finding Ore: A Tutorial on Using the Method in Geological Remote Sensing. *IEEE Geosci. Remote Sens. Mag.* **2019**, *7*, 51–71. [CrossRef]
41. Demetriades-Shah, T.H.; Steven, M.D.; Clark, J.A. High resolution derivative spectra in remote sensing. *Remote Sens. Environ.* **1990**, *33*, 55–64. [CrossRef]
42. Kariuki, P.C.; Woldai, T.; van der Meer, F. Effectiveness of spectroscopy in identification of swelling indicator clay minerals. *Int. J. Remote Sens.* **2004**, *25*, 455–469. [CrossRef]
43. Poggialini, F.; Legnaioli, S.; Campanella, B.; Cocciaro, B.; Lorenzetti, G.; Raneri, S.; Palleschi, V. Calculating the Limits of Detection in Laser-Induced Breakdown Spectroscopy: Not as Easy as It Might Seem. *Appl. Sci.* **2023**, *13*, 3642. [CrossRef]
44. Gomez, C.; Adeline, K.; Bacha, S.; Driessen, B.; Gorretta, N.; Lagacherie, P.; Roger, J.M.; Briottet, X. Sensitivity of clay content prediction to spectral configuration of VNIR/SWIR imaging data, from multispectral to hyperspectral scenarios. *Remote Sens. Environ.* **2018**, *204*, 18–30. [CrossRef]
45. Currie, L.A. Detection and quantification limits: Origins and historical overview. *Anal. Chim. Acta* **1999**, *391*, 127–134. [CrossRef]
46. Vogelgesang, J.; Haedrich, J. Limits of Detection, Identification and Determination: A Statistical Approach for Practitioners. *Accredit. Qual. Assur.* **1998**, *3*, 242–255. [CrossRef]
47. Wu, X.; Mustard, J.F.; Tarnas, J.D.; Zhang, X.; Das, E.; Liu, Y. Imaging Mars analog minerals' reflectance spectra and testing mineral detection algorithms. *Icarus* **2021**, *369*, 114644. [CrossRef]

48. Wu, X.; Zhang, X.; Mustard, J.; Tarnas, J.; Lin, H.; Liu, Y. Joint Hapke Model and Spatial Adaptive Sparse Representation with Iterative Background Purification for Martian Serpentine Detection. *Remote Sens.* **2021**, *13*, 500. [CrossRef]
49. Santamaría-López, A.; Suárez, M.; García-Romero, E. Detection limits of kaolinites and some common minerals in binary mixtures by short-wave infrared spectroscopy. *Appl. Clay Sci.* **2024**, *250*, 107269. [CrossRef]
50. Moore, D.M.; Reynolds, R.C., Jr. *Diffraction and the Identification and Analysis of Clay Minerals*, 2nd ed.; Oxford University Press: New York, NY, USA, 1997.
51. Warr, L.N. IMA–CNMNC approved mineral symbols. *Mineral. Mag.* **2021**, *85*, 291–320. [CrossRef]
52. García-Romero, E.; Manchado, E.M.; Suárez, M.; García-Rivas, J. Spanish bentonites: A review and new data on their geology, mineralogy, and crystal chemistry. *Minerals* **2019**, *9*, 696. [CrossRef]
53. Manchado, E.M.; Suárez, M.; García-Romero, E. The kaolin and bentonite deposit of Tamame de Sayago (Zamora, Spain): Mineralogy, geochemistry, and genesis. *Clays Clay Miner.* **2023**, *71*, 478–495. [CrossRef]
54. García-Romero, E.; Suárez, M. HRTEM evidence of Tajo Basin mineralogical complexity: Crystal chemistry and genetic relationship. *Appl. Clay Sci.* **2022**, *224*, 106515. [CrossRef]
55. García-Rivas, J.; Suárez, M.; García-Romero, E.; García-Meléndez, E. Identification and classification of mineralogical associations by VNIR-SWIR spectroscopy in the Tajo basin (Spain). *Int. J. Appl. Earth Obs. Geoinf.* **2018**, *72*, 57–65. [CrossRef]
56. Iyakwari, S.; Glass, H.J. Influence of mineral particle size and choice of suitable parameters for ore sorting using near infrared sensors. *Miner. Eng.* **2014**, *69*, 102–106. [CrossRef]
57. Menges, F. Spectragryph-Optical Spectroscopy Software (Version 1.2.15). 2016. Available online: http://www.effemm2.de/spectragryph/ (accessed on 19 September 2024).
58. Cardoso-Fernandes, J.; Silva, J.; Dias, F.; Lima, A.; Teodoro, A.C.; Barrès, O.; Cauzid, J.; Perrotta, M.; Roda-Robles, E.; Ribeiro, M.A. Tools for remote exploration: A lithium (Li) dedicated spectral library of the Fregeneda–Almendra aplite–pegmatite field. *Data* **2021**, *6*, 33. [CrossRef]
59. Gaffey, S.J. Spectral reflectance of carbonate minerals in the visible and near infrared (0.35-2.55 microns): Calcite, aragonite, and dolomite. *Am. Mineral.* **1986**, *71*, 151–162. [CrossRef]
60. Rinnan, A.; Van den Berg, F.; Engelsen, S.B. Review of the most common pre-processing techniques for near-infrared spectra. *TrAC Trends Anal. Chem.* **2009**, *28*, 1201–1222. [CrossRef]
61. Clark, R.N. Chapter 1: Spectroscopy of rocks and minerals, and principles of spectroscopy. In *Remote Sensing for the Earth Sciences: Manual of Remote Sensing*; Rencz, N.A., Ed.; John Wiley & Sons: New York, NY, USA, 1999; pp. 3–58.
62. Mulder, V.L.; Plötze, M.; de Bruin, S.; Schaepman, M.E.; Mavris, C.; Kokaly, R.F.; Egli, M. Quantifying mineral abundances of complex mixtures by coupling spectral deconvolution of SWIR spectra (2.1–2.4 μm) and regression tree analysis. *Geoderma* **2013**, *207–208*, 279–290. [CrossRef]
63. Squyres, S.W.; Arvidson, R.E.; Bell, J.F.; Calef, F.; Clark, B.C.; Cohen, B.A.; Crumpler, L.A.; de Souza, P.A.; Farrand, W.H.; Gellert, R.; et al. Ancient Impact and Aqueous Processes at Endeavour Crater, Mars. *Science* **2012**, *336*, 570–576. [CrossRef]
64. Zhang, G.; Wasyliuk, K.; Pan, Y. The characterization and quantitative analysis of clay minerals in the Athabasca basin, Saskatchewan: Application of shortwave infrared reflectance spectroscopy. *Can. Mineral.* **2001**, *39*, 1347–1363. [CrossRef]
65. Bou-Orm, N.; Al Romaithi, A.A.; Elrmeithi, M.; Ali, F.M.; Nazzal, Y.; Howari, F.M.; Al Aydaroos, F. Advantages of first-derivative reflectance spectroscopy in the VNIR-SWIR for the quantification of olivine and hematite. *Planet. Space Sci.* **2020**, *188*, 104957. [CrossRef]
66. Ducasse, E.; Adeline, K.; Briottet, X.; Hohmann, A.; Bourguignon, A.; Grandjean, G. Montmorillonite estimation in clay-quartz-calcite samples from laboratory SWIR imaging spectroscopy: A comparative study of spectral preprocessings and unmixing methods. *Remote Sens.* **2020**, *12*, 1723. [CrossRef]
67. McKeown, N.K.; Bishop, J.L.; Cuadros, J.; Hillier, S.; Amador, E.; Makarewicz, H.D.; Parente, M.; Silver, E.A. Interpretation of reflectance spectra of clay mineral-silica mixtures: Implications for Martian clay mineralogy at Mawrth Vallis. *Clays Clay Miner.* **2011**, *59*, 400–415. [CrossRef]
68. Mathian, M.; Hebert, B.; Baron, F.; Petit, S.; Lescuyer, J.; Furic, R.; Beaufort, D. Identifying the phyllosilicate minerals of hypogene ore deposits in lateritic saprolites using the near-IR spectroscopy second derivative methothology. *J. Geochem. Explor.* **2018**, *186*, 198–314. [CrossRef]
69. Hubbard, B.E.; Gallegos, T.J.; Stengel, V.; Hoefen, T.M.; Kokaly, R.F.; Elliott, B. Hyperspectral (VNIR-SWIR) analysis of roll front uranium host rocks and industrial minerals from Karnes and Live Oak Counties, Texas Coastal Plain. *J. Geochem. Explor.* **2024**, *257*, 107370. [CrossRef]
70. Ali, A.; Chiang, Y.W.; Santos, R.M. X-ray Diffraction Techniques for Mineral Characterization: A Review for Engineers of the Fundamentals, Applications, and Research Directions. *Minerals* **2022**, *12*, 205. [CrossRef]
71. Hapke, B. Bidirectional reflectance spectroscopy. *5. The coherent backscatter opposition effect and anisotropic scattering. Icarus* **2002**, *157*, 523–534. [CrossRef]

Disclaimer/Publisher's Note: The statements, opinions and data contained in all publications are solely those of the individual author(s) and contributor(s) and not of MDPI and/or the editor(s). MDPI and/or the editor(s) disclaim responsibility for any injury to people or property resulting from any ideas, methods, instructions or products referred to in the content.